The Planetary Science Journal, 2:21 (12pp), 2021 February https://doi.org/10.3847/PSJ/abd71d

Quantifying the Hypervolatile Abundances in Jupiter-family Comet 46P/Wirtanen

Adam J. McKay[1,2,9], Michael A. DiSanti[1,3,9], Anita L. Cochran[4], Boncho P. Bonev[2,9], Neil Dello Russo[5,9], Ronald J. Vervack, Jr.[5,9], Erika Gibb[6,9], Nathan X. Roth[1,7], Mohammad Saki[6,9], Younas Khan[6,9], and Hideyo Kawakita[8,9]

[1] NASA Goddard Space Flight Center, Solar System Exploration Division Code 690, Greenbelt, MD 20771, USA; adam.mckay@nasa.gov
[2] Department of Physics, American University, 4400 Massachusetts Avenue NW, Washington, DC 20016, USA
[3] Goddard Center for Astrobiology, NASA-Goddard Space Flight Center, Greenbelt, MD 20771, USA
[4] University of Texas at Austin/McDonald Observatory, 2515 Speedway, Stop C1402, Austin, TX 78712, USA
[5] Johns Hopkins University, Applied Physics Laboratory, 11100 Johns Hopkins Road, Laurel, MD 20723, USA
[6] Department of Physics, 1 University Boulevard, University of Missouri–St.Louis, St. Louis, MO 63121, USA
[7] Universities Space Research Association, Columbia, MD, USA
[8] Koyama Astronomical Observatory, Kyoto Sangyo University Motoyama, Kamigamo, Kita-ku, Kyoto, 603-8555, Japan
Received 2020 September 30; revised 2020 December 8; accepted 2020 December 26; published 2021 February 4

Abstract

We present analysis of IR and optical spectroscopy of Jupiter-family comet (JFC) 46P/Wirtanen obtained in 2019 January, when the comet had sufficient geocentric velocity to enable studies of the hypervolatiles CO and CH_4, as well as [O I] emission. These species could not be studied near closest approach in mid-December because there was insufficient Doppler shift to separate the cometary emission from their corresponding telluric absorption lines. We employed the [O I] observations as a proxy for the CO_2/H_2O ratio, as CO_2 cannot be observed directly from the ground, and space-based assets sensitive to CO_2 were not able to observe 46P during this apparition. We focused our analysis on H_2O, CO, CH_4, C_2H_6, CH_3OH, and CO_2 (via [O I] emission). We detected strong emissions from H_2O, C_2H_6, and CH_3OH. Over the 3 nights, we found evidence for changing mixing ratios, mostly due to a variable H_2O production rate. In 46P, C_2H_6 and CH_3OH are enriched compared to cometary averages, with mixing ratios relative to H_2O of ∼1% and ∼3%, respectively. Measurements of CH_4 and CO have been especially rare in JFCs. We report significant 3σ upper limits on $CH_4/H_2O < 0.97\%$ and $CO/H_2O < 0.54\%$. They place CH_4 being near-average or depleted, and CO being strongly depleted in 46P compared with Oort cloud comets. 46P has comparable CO/H_2O to the few other measurements in JFCs, but enriched in C_2H_6 and CH_3OH. Our inferred CO_2/H_2O mixing ratio is ∼15%, though accounting for systematic uncertainties from the lack of knowledge of [O I] photochemistry means a value between 10% and 20% is likely. The compositional profile of 46P is similar to another small, hyperactive comet: 103P/Hartley 2. The mechanism of CO_2-driven water-rich ice grain production proposed for 103P/Hartley 2 may be operating on 46P as well.

Unified Astronomy Thesaurus concepts: Comets (280); Comae (271); Comet volatiles (2162); Short period comets (1452)

1. Introduction

Comets represent primitive material left over from the formation of the solar system. As such, they are invaluable tools for understanding the physical and chemical processes operating during the solar system's earliest stages. Although they have spent most of the 4.5 billion yr since the formation of the solar system stored in the scattered disk and Oort Cloud, comets also experience heating from their close perihelion passages in the inner solar system. Observations of hypervolatile species, those species with low vacuum sublimation temperatures (<50 K), in different dynamical classes can help constrain the effect of repeated perihelion passages on observed cometary composition. Hypervolatiles typically observed in comets via ground-based observations include CO, CH_4, and C_2H_6 (Dello Russo et al. 2016). Also abundant is CO_2, but it can only be directly observed from space due to severe telluric absorption (Ootsubo et al. 2012; Reach et al. 2013; McKay et al. 2016, 2019).

Observations of CO, CH_4, and C_2H_6 have been obtained for over 30 comets (Dello Russo et al. 2016; Bockelée-Morvan & Biver 2017), though most of these comets have an Oort Cloud origin (Oort Cloud comets, OCCs). This leaves a paucity of observations for these molecules in Jupiter-family comets (JFCs), comets that have likely experienced the most thermal alteration due to repeated perihelion passages. This is especially true for CO and CH_4 at IR wavelengths, for which, as of a few years ago, fewer than five measurements in JFCs existed (Dello Russo et al. 2016). This lack of observations is due to the fact that significant geocentric velocity ($>10\,km\,s^{-1}$) is needed to Doppler shift cometary emissions away from corresponding telluric absorptions to wavelengths of sufficient atmospheric transmittance in order to be measured. Due to their generally low activity levels, observations of JFCs at IR wavelengths are usually only possible near closest approach to Earth, when the geocentric velocity is insufficient for targeting CO and CH_4. The last several years presented extremely rare and favorable opportunities to observe hypervolatiles in JFCs, greatly increasing the number of JFCs with measured CH_4 and CO abundances (DiSanti et al. 2017; Dello Russo et al. 2020;

[9] Visiting Astronomer at the Infrared Telescope Facility, which is operated by the University of Hawaii under contract NNH14CK55B with the National Aeronautics and Space Administration.

Table 1
Observation Log

UT Date	R_h (au)	$\dot{R}_h$ (km s^{-1})	Δ (au)	$\dot{\Delta}$ (km s^{-1})	Tell. Standard	Flux Standard
NASA IRTF iSHELL						
2019 Jan 11	1.13	+8.1	0.18	+10.1	HR 4905	HR 4905
2019 Jan 12	1.13	+8.3	0.18	+10.3	HR 4905	HR 4905
2019 Jan 13	1.14	+8.5	0.19	+10.4	HR 4905	HR 4905
McDonald coudé						
2019 Jan 8	1.11	+7.4	0.16	+9.8	HR 189	HR 153

Faggi et al. 2019; Paganini et al. 2019; Roth et al. 2018; Roth et al. 2020).

For CO_2, there is more balance between OCCs and JFCs, though there is little overlap of CO_2 observations with studies of other volatiles. Contemporaneous observations of CO and CO_2 exist from a survey of 18 comets observed by the AKARI spacecraft (Ootsubo et al. 2012), but only two of these comets had detections of both CO and CO_2, and neither of these comets was a JFC.

The CO_2 can also be studied indirectly via [O I] emission. The flux ratio of the [O I] 5577 Å line to the sum of the [O I] 6300 and [O I] 6364 Å lines (hereafter referred to as the oxygen line ratio) is potentially sensitive to the CO_2 abundance in comets (Festou & Feldman 1981; McKay et al. 2012, 2013; Decock et al. 2013). However, the photochemistry responsible for [O I] release into cometary comae is not fully understood (Huestis et al. 2008; Bhardwaj & Raghuram 2012), limiting the usefulness of the oxygen line ratio as a proxy for CO_2 in comets. Recently derived empirical release rates have had some success in reproducing observed CO_2 abundances (McKay et al. 2015, 2016).

The JFC 46P/Wirtanen made a historic close approach to Earth in 2018 mid-December, allowing for detailed study from Earth-based facilities. In addition to being a JFC, 46P was the original target of the Rosetta mission and is often considered a target for future missions. The 2018–2019 apparition provided powerful opportunities for study, including the ability to observe CO and CH_4 in a JFC. This was not possible around closest approach and perihelion in mid-December due to insufficient Doppler shift, but CO and CH_4 observations were possible several weeks later in 2019 January. Although the Spitzer Space Telescope and NEOWISE were in operation and can observe CO_2 in comets (Reach et al. 2013; Bauer et al. 2015; McKay et al. 2016, 2019), unfortunately, in the months around perihelion, 46P was not located in the observing annulus for either of these facilities, meaning direct CO_2 observations were not possible. However, the observing geometry was conducive to [O I] observations, which can be used as an indirect proxy for CO_2.

We present analysis of IR and optical spectroscopy of 46P obtained in 2019 January, with a focus on the hypervolatiles CO, CH_4, and C_2H_6, as well as CO_2 (through [O I] emission). We also present results for CH_3OH and H_2O as links to observations near perihelion in 2018 December. Section 2 discusses our observations and data reduction procedures. Section 3 details our results, with Section 4 providing a comparison to other comets and discussion of the implications of our results. Section 5 concludes the paper.

2. Observations and Data Analysis

We obtained IR observations using the iSHELL instrument on the NASA Infrared Telescope Facility (IRTF) and optical spectroscopy using the Tull coudé spectrograph on the Harlan J. Smith 2.7 m Telescope at McDonald Observatory. Table 1 provides the details of these observations.

2.1. NASA IRTF iSHELL

2.1.1. Observations

The iSHELL instrument is a cross-dispersed IR spectrometer with sensitivity over the ~1–5 μm wavelength range. More details on iSHELL can be found in Rayner et al. (2012, 2016). For the comet observations, we used the 0.″75 wide slit, which provides a spectral resolving power of $R \equiv \frac{\lambda}{\Delta\lambda} \sim 38,000$ for a uniform monochromatic source. We also observed an early-type IR standard star with the 4″ wide slit to serve as a flux calibrator and telluric standard (see Section 2.1.2). This observation setup provides lower spectral resolution for the standard star observations ($R \sim 20{,}000$) but minimizes slit losses and therefore systematic errors in flux calibration. Both the comet and standard star were observed using the ABBA nodding sequence, in which the comet position is rotated through two different positions in the slit (A and B positions) and observations are taken in the order ABBA, in order to facilitate subtraction of the background sky during reduction of the data. We used a 7.″5 telescope nod (half the slit length) along the slit between the A and B positions. We observed using several grating settings: M2, Lp1, and our own custom *L*-band setting, Lcustom. Setting M2 covers a wavelength range of ~4.52–5.25 μm, encompassing spectral lines of CO and H_2O. Setting Lp1 encompasses wavelengths around 3.3 μm and samples emission lines from CH_4, C_2H_6, and CH_3OH. Setting Lcustom covers the 3 μm region and provides access to the strongest H_2O lines. Settings observed and time on source for each observation date are provided in Table 2. We obtained flats and darks at the end of each observing sequence for each grating setting, prior to resetting the instrument.

The slit was oriented along the comet–Sun vector projected on the plane of the sky (position angle 203°). Guiding was achieved through a filter imaging in the *J* band with the slit viewer camera. The slit viewer allows active guiding on sufficiently bright targets while obtaining spectra, and both 46P and our standard star were bright enough for this purpose. Short-timescale guiding was achieved through a boresight guiding technique, which utilizes "spillover" flux that falls outside the slit jaws to keep the optocenter on the slit. More details relevant to cometary observations using iSHELL are presented in DiSanti et al. (2017).

Table 2
iSHELL Grating Settings

UT Date	Setting	Wavenumber Range (cm^{-1})	Species	UT Time Start–Finish	Time on Source (minutes)
1/11/19	M2	1905–2212	H_2O, CO	9:29–11:51	107
	Lp1	2740–3049	C_2H_6, CH_3OH, CH_4	11:53–14:03	116
	Lcustom	3220–3530	H_2O	14:13–15:14	52
1/12/19	Lp1	2740–3049	C_2H_6, CH_3OH, CH_4	9:39–11:51	116
	M2	1905–2212	H_2O, CO	11:52–13:48	136
1/13/19	M2	1905–2212	H_2O, CO	9:28–11:04	74
	Lcustom	3220–3530	H_2O	11:06–13:04	104
	Lp1	2740–3049	C_2H_6, CH_3OH, CH_4	13:10–14:04	48

2.1.2. Reduction and Data Analysis

We applied our general methodology for processing IR spectra (e.g., Dello Russo et al. 2006; Villanueva et al. 2011a; DiSanti et al. 2014). This process yielded an extracted 1D spectrum for both the reference star and comet. We fit a synthetic atmospheric transmittance model to the standard star spectrum and applied this optimized atmospheric transmittance model to the comet spectrum. Correcting for transmittance and incorporating flux calibration factors from our standard star spectra allowed for establishing line fluxes incident at the top of the Earth's atmosphere.

We established molecular column densities (or upper limits) by dividing these transmittance-corrected line fluxes by appropriate line-specific fluorescence g-factors, the values of which depend on rotational temperature (T_{rot}; see Gibb et al. 2003; Radeva et al. 2011; Villanueva et al. 2011b, 2012b, 2012a; Paganini et al. 2013 for more details on the basis of these calculations). To obtain molecular production rates, we extracted a "nucleus-centered" spectrum by summing signal over 15 rows (∼2.″5) centered on the row containing the peak emission line intensity. We employed a Haser model combined with appropriate g-factors to derive the nucleus-centered production rate, Q_{nc} (Haser 1957; Dello Russo et al. 1998). We adopt a gas expansion velocity relation with a heliocentric distance dependence of $0.8R_h^{-0.5}$ (Biver et al. 1999; Bonev et al. 2005), which for our observations corresponds to $\sim 0.75\ km\ s^{-1}$ (this is the same as adopted for our [O I] measurements; Section 2.2). The resulting production rates depend linearly on the adopted expansion velocity as our measurements occur in the inner coma, and, as we assume the expansion velocity is the same for all species, there is no dependence of the derived mixing ratios on the adopted expansion velocity (DiSanti et al. 2017). Photodissociation timescales (at $R_h = 1$ au) are 8.3×10^4 s for H_2O, 1.3×10^6 s for CO, 1.3×10^5 s for CH_4, and 1.0×10^5 s for C_2H_6 and CH_3OH (Huebner et al. 1992), and we scale these to the heliocentric distance of our observations using an R_h^2 dependence.

Owing primarily to seeing, Q_{nc} invariably underestimates the actual "total" (or "global") production rate, Q_{tot}. To obtain Q_{tot}, we multiplied each Q_{nc} by an appropriate growth factor (GF), determined through the well-documented "Q-curve" method for analyzing spatial profiles of emissions (Dello Russo et al. 1998). For each spatial step, a "symmetrized" Q-curve was produced by averaging signal at equal but diametrically opposed distances from the nucleus.

Uncertainties on the nucleus-centered production rates include both stochastic noise and a 5% uncertainty in flux calibration due to factors such as slit losses, inaccurate stellar parameters, etc. (DiSanti et al. 2017). Global production rates include uncertainties in the GF as well. Mixing ratios for species observed in different settings (e.g., C_2H_6/H_2O) were calculated using global production rates, as they are not observed simultaneously. Therefore, we include uncertainties from both flux calibration and GF analysis in the quoted uncertainties. However, for species observed in the same setting (e.g., CO/H_2O), they are observed simultaneously. Therefore, flux calibration and GF analysis uncertainties are not included.

2.2. McDonald Observatory Tull Coudé

2.2.1. Observations

Three days before our IRTF observations, we obtained optical spectra of 46P with the Tull coudé instrument, mounted on the 2.7 m Harlan J. Smith Telescope at McDonald Observatory. This instrument provides high spectral resolving power ($R = 60{,}000$), which is critical for studies of [O I] emission. The spectra cover a wavelength range of 3500–10000 Å. This coverage is complete blueward of 5700 Å, with increasing interorder gaps redward of this value (the [O I] 6300 and [O I] 6364 Å lines do not fall in these gaps for our observations). The slit is 1.″2 × 8.″2. More details about the Tull coudé can be found elsewhere (Tull et al. 1995).

We tracked the comet nonsidereally using an ephemeris from the JPL Horizons service, and short-term guiding was achieved using a boresight technique similar to that employed for the iSHELL observations. We obtained four spectra of the optocenter of the comet, each with an 1800 s integration time. In our experience, we have found that this exposure time optimizes the signal-to-noise ratio in the spectra while ensuring that cosmic-ray events do not have a significant adverse effect on the spectra.

In addition to the comet, we observed standard stars for the purposes of flux calibration and removal of telluric absorptions and solar continuum/solar absorption lines. We observed the flux standard HR 153 for the purposes of flux calibration and the fast-rotating early-type star HR 189 for removal of telluric absorptions. The Tull coudé has the ability to observe the solar spectrum using daylight that is fed directly into the instrument through a solar port. Therefore, we use the actual solar spectrum rather than a solar analog in order to remove the solar continuum and absorption lines from the comet spectra. We also obtained observations of quartz and ThAr lamps for flat-fielding and wavelength calibration, respectively.

2.2.2. Reduction and Data Analysis

We summed the comet spectra as echellograms (i.e., before spectral extraction to 1D spectra). This was done because removing radiation events is more effective with this approach rather than removing radiation events from the individual spectra. We performed bias subtraction, flat-fielding, wavelength calibration, and spectral extraction using IRAF. We then applied the standard star and solar port observations for flux calibration and removal of the telluric and solar contributions to the comet spectrum. Due to the narrow nature of the Tull coudè slit, only a fraction of the star's light actually enters the slit. We determined these slit losses for the flux standard star observations by performing aperture photometry on the slit viewer images as described in McKay et al. (2014). Slit losses introduce a systematic error in the flux calibration of ∼17% that dominates over the stochastic noise. For more details concerning the reduction techniques, see Cochran & Cochran (2002) and McKay et al. (2012).

We fit the cometary and telluric [O I] lines to Gaussian profiles using the methodology of McKay et al. (2012, 2013) in order to derive observed fluxes. It was necessary to include the telluric line in the model fit because, even though the geocentric velocity was sufficient at the Tull coudé resolution to resolve the line centers, there was still overlap between the line profiles.

We used the [O I] 6300 Å line flux as a proxy for H_2O production, as has been done in the past with success (e.g., Morgenthaler et al. 2001; Fink 2009; McKay et al. 2014, 2020). We used a Haser model with scale lengths modified to emulate the vectorial model originally developed by Morgenthaler et al. (2001) and adapted for slit spectroscopy (McKay et al. 2012, 2014).

To convert the observed oxygen line ratio to an inferred CO_2/H_2O ratio, we use the following equation (McKay et al. 2012):

$$\frac{N_{CO_2}}{N_{H_2O}} = \frac{RW_{H_2O}^{red} - W_{H_2O}^{green}}{W_{CO_2}^{green} - RW_{CO_2}^{red}}, \quad (1)$$

where N is the column density and R is the oxygen line ratio. The release rate W is defined as

$$W \equiv \tau^{-1}\alpha\beta, \quad (2)$$

where τ represents the photodissociative lifetime of the parent molecule, α is the yield into the excited state of interest, and β represents the branching ratio for a given line out of a certain excited state.

As discussed in Section 1, the release rates, W, are not well constrained from laboratory measurements. McKay et al. (2015) used observations of comet C/2009 P1 (Garradd) in order to derive empirical values for W so that the measured CO_2/H_2O ratio could be reproduced from the [O I] observations via Equation (1). These rates were then applied to observations of C/2012 K1 (PanSTARRS), which reproduced the observed CO_2/H_2O ratio to an accuracy of 20% (McKay et al. 2016). We employed these empirical release rates, which are shown in Table 3, to infer the CO_2/H_2O ratio in 46P. We discuss the systematic uncertainties associated with this approach in Section 3.2. We ignored the contribution of CO, as it has been shown to be inefficient at supplying the [O I] population (Raghuram et al. 2020), especially at the low CO abundances we find for 46P (see Section 3.1.3).

Table 3
Adopted O I Release Rates for Inferring CO_2/H_2O

Parent	O I State	W^a	W^b
H_2O	^1S	0.64	0.64
H_2O	^1D	84.4	84.4
CO_2	^1S	50.0	33.0
CO_2	^1D	75.0	49.5

Notes.
[a] Empirical release rates A from McKay et al. (2015) in 10^{-8} s^{-1}.
[b] Empirical release rates B from McKay et al. (2015) in 10^{-8} s^{-1}.

Before the oxygen line ratio can be inserted into Equation (1), it must be corrected for the effects of collisional quenching. The ^1D state responsible for the [O I] 6300 and [O I] 6364 Å emissions has a lifetime of approximately 110 s, and an O I atom in this state can be collisionally de-excited before it emits a photon for typical number densities in cometary comae. However, the ^1S state responsible for the [O I] 5577 Å line has a much shorter lifetime of ∼1 s and does not undergo significant collisional de-excitation in cometary comae. Therefore, the [O I] 6300 and [O I] 6364 Å flux lost to collisions must be accounted for. We use the H_2O production rate combined with our Haser model for O I to calculate the expected flux lost to collisions following the methodology of McKay et al. (2015). This provides a correction factor that is applied to the measured oxygen line ratio before being utilized in Equation (1).

3. Results

3.1. IR: CO, CH_4, C_2H_6, CH_3OH, and H_2O

3.1.1. Rotational Temperatures

We present our adopted rotational temperatures T_{rot} in Table 4. For the present study, only C_2H_6 in Lp1 and H_2O in Lcustom presented enough lines with high S/N that spanned a sufficient range of rotational energy to obtain a robust measure of T_{rot}. Our analysis of C_2H_6 provided a best-fit value T_{rot} = 66–73 K, depending on the date, with H_2O in Lcustom providing similar values. Therefore, we adopted the rotational temperature obtained from C_2H_6 for all species observed in M2 or Lp1, and for H_2O emission in Lcustom, we adopted the measured value of T_{rot} from the H_2O lines (assumed values have no uncertainties in Table 4). This is also justified by past observations of brighter comets in which T_{rot} values measured for multiple species are consistent (e.g., Dello Russo et al. 2011; Mumma et al. 2011; Gibb et al. 2012; DiSanti et al. 2014).

3.1.2. Spatial Analysis

We obtained GFs for C_2H_6 and H_2O emissions (in both the M2 and Lcustom settings), as these were the only lines bright enough for reliable GFs to be measured. We show the measured GFs in Table 4. For the other species, we adopted the GF for the emission observed in the same spectral setting, as emissions in the same setting are observed simultaneously and should be affected similarly by observational conditions contributing to the GF. As with the values of T_{rot}, assumed GF values do not have uncertainties in Table 4.

Of the species observed, only C_2H_6 and H_2O emission from the Lcustom setting were bright enough for high-S/N spatial

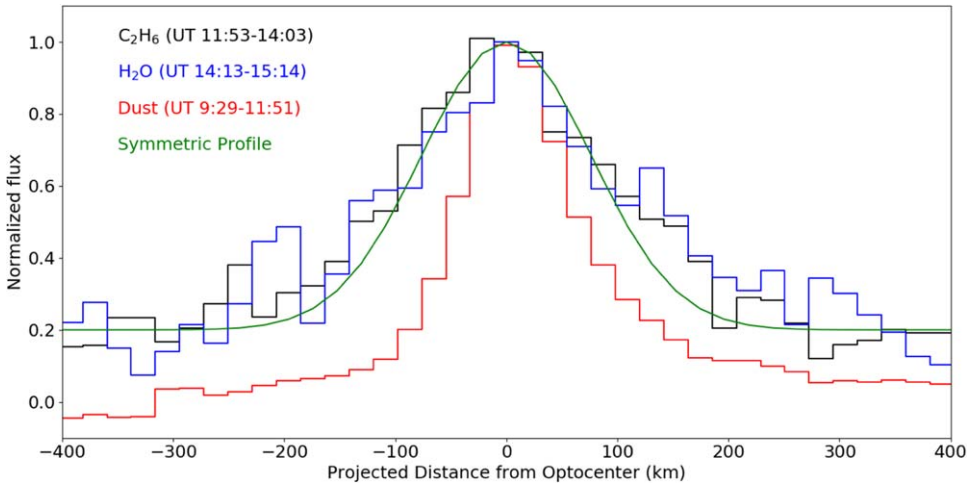

Figure 1. Spatial profiles of C_2H_6 (black), H_2O (blue), and the dust continuum (red) on UT January 11. The H_2O profile is taken from the Lcustom setting, as these observations had a higher S/N. The green curve represents a symmetric Gaussian profile to guide the eye (i.e., it does not represent a fit to the data). The positive *x*-direction denotes the projected antisolar direction. All curves are normalized so that their peak value is unity. The dust profile is much narrower than the gas profiles, as previously observed in both 46P and other comets, and both the H_2O and C_2H_6 profiles are similar to each other. The dust profile is clearly asymmetric toward the projected antisolar direction, and there is also tentative evidence for an extension in the antisolar direction for the gaseous species as well (compare to the green curve, which represents a symmetric profile).

Table 4
Production Rates and Abundances

UT Date	Setting	Species	T_{rot}	Q_{nc} (10^{25} mol s^{-1})	GF	Q_{tot} (10^{25} mol s^{-1})	X/H_2O (%)	X/C_2H_6
1/11/2019	M2	H_2O	67	354 ± 25	1.61 ± 0.05	570 ± 43	100	148 ± 14
		CO	67	<1.92	1.61	<3.09	<0.54	<0.82
	Lp1	C_2H_6	67 ± 2	2.50 ± 0.13	1.54 ± 0.04	3.85 ± 0.22	0.68 ± 0.06[a] 0.93 ± 0.09[b]	1
		CH_3OH	67	8.11 ± 0.47	1.54	12.5 ± 0.79	2.19 ± 0.22[a] 3.03 ± 0.30[b]	3.24 ± 0.10
		CH_4	67	<3.60	1.54	<5.55	<0.97[a] <1.35[b]	<1.44
	Lcustom	H_2O	72 ± 6	242 ± 13	1.70 ± 0.10	412 ± 32	100	108 ± 11
1/12/2019	Lp1	C_2H_6	73 ± 2	2.36 ± 0.12	1.67 ± 0.05	3.94 ± 0.23	1.01 ± 0.13	1
		CH_3OH	73	7.17 ± 0.44	1.67	12.0 ± 0.8	3.08 ± 0.41	3.04 ± 0.11
		CH_4	73	<3.66	1.67	<6.11	<1.57	<1.55
	M2	H_2O	73	256 ± 15	1.52 ± 0.15	389 ± 44	100	99 ± 13
		CO	73	<2.13	1.52	<3.24	<0.84	<0.92
1/13/2019	M2	H_2O	66	233 ± 22	1.51 ± 0.12	352 ± 44	100	83 ± 13
		CO	66	<2.15	1.51	<3.25	<0.92	<0.76
	Lcustom	H_2O	66 ± 4	276 ± 16	1.54 ± 0.04	425 ± 22	100	100 ± 9
	Lp1	C_2H_6	66 ± 3	2.42 ± 0.13	1.76 ± 0.13	4.26 ± 0.39	1.00 ± 0.09[b]	1
		CH_3OH	66	7.91 ± 0.56	1.76	13.9 ± 1.4	3.27 ± 0.37[b]	3.27 ± 0.17
		CH_4	66	<7.95	1.76	<14.0	<3.29[b]	<3.31

Notes.
[a] Relative to H_2O measured in M2.
[b] Relative to H_2O measured in Lcustom.

profiles with the potential to reveal any asymmetries in outgassing to be derived (the H_2O emission in M2, while of sufficient S/N for derivation of a GF, was not a high enough S/N for this purpose). While our observations only cover the very inner coma, significant asymmetries have been observed over similar spatial scales in other comets (e.g., Dello Russo et al. 2011; Villanueva et al. 2011a; Bonev et al. 2014; DiSanti et al. 2017; Roth et al. 2018). We show the spatial profile for H_2O and C_2H_6, as well as the dust continuum, in Figure 1. The dust continuum is clearly asymmetric in the projected antisolar direction (positive *x*-values), and there is tentative evidence that the gaseous profiles may also be asymmetric in the same direction (compare to the green curve in Figure 1, which represents a symmetric profile). This is similar to the spatial profiles observed for both species near perihelion in 2018 December (Roth et al. 2020; Bonev et al. 2021; Khan et al. 2021). However, near perihelion, the H_2O spatial profile was more extended than C_2H_6, which was interpreted as evidence for an extended source of H_2O production. Rather than this extended source disappearing between perihelion and our observations, it is more likely that the increase in geocentric distance by a factor of 2 between December and January and

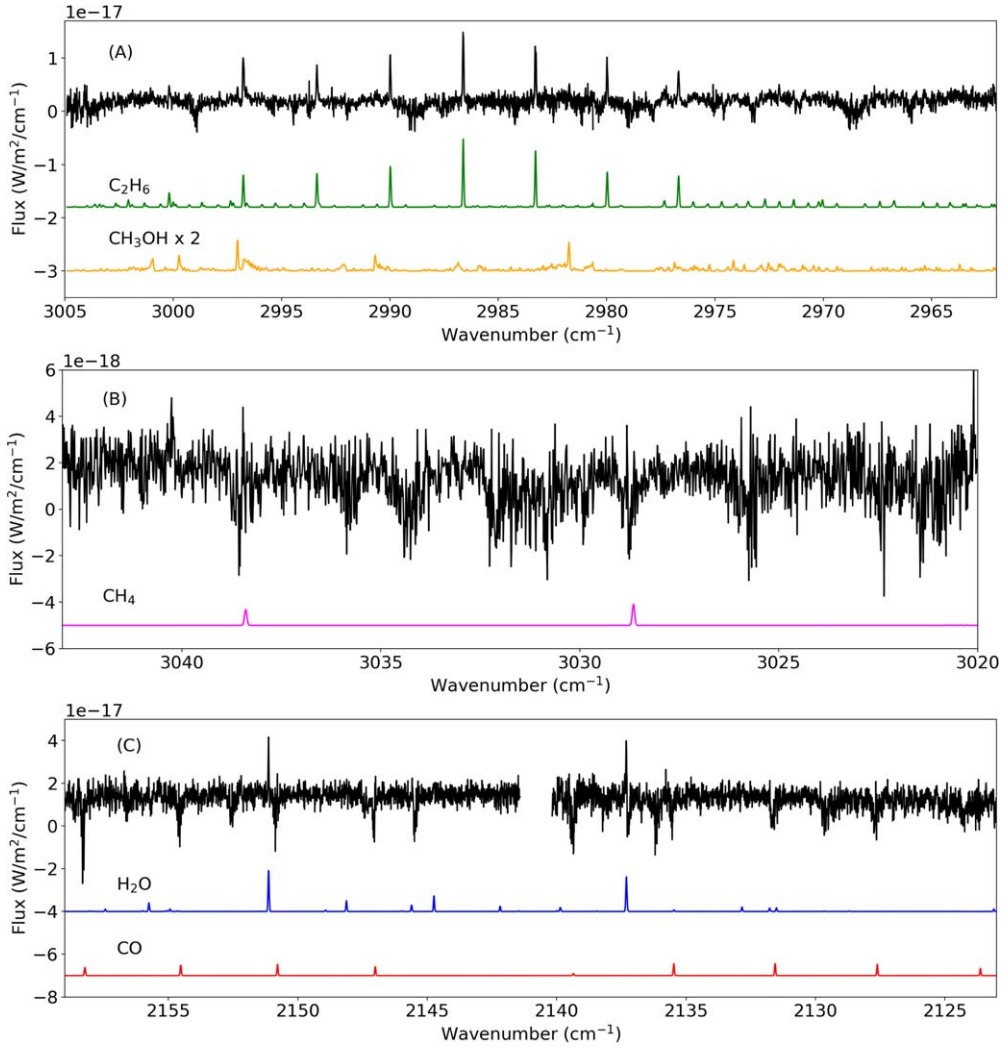

Figure 2. IR spectra from UT January 11 showing spectral regions containing C_2H_6 and CH_3OH (panel (a)), CH_4 (panel (b)), and CO and H_2O (panel (c)) emissions. Data are shown in black, with model fits for specific species offset below the spectra. The CH_3OH model has been multiplied by a factor of 2 for clarity. The spectra show strong detections of H_2O, CH_3OH, and C_2H_6 and nondetections of CH_4 and CO. The model fits for CO and CH_4 are shown to depict the expected positions of the CH_4 lines.

the resulting loss of spatial resolution in the very inner coma mean that we are no longer resolving the extended source of H_2O production. Spatial profiles for C_2H_6, H_2O, and the dust continuum are similar on UT January 12 and January 13 to those shown in Figure 1, albeit at a lower S/N for one or both species due to less time on source (see Table 2).

3.1.3. Production Rates and Mixing Ratios

We present our nucleus-centered production rates Q_{nc}, global production rates Q_{tot}, and mixing ratios (abundance ratios) compared to H_2O and C_2H_6 in Table 4. The spectral settings are shown in the order in which they were observed on each date (see Table 2 for UT time ranges). Example spectra from UT January 11 are shown in Figures 2 and 3. We obtained strong detections of C_2H_6, CH_3OH, and H_2O (in both the M2 and Lcustom settings) and 3σ upper limits on CH_4 and CO.

The water production as measured in the M2 setting was approximately 50% higher on UT January 11 than on the following 2 days, whereas C_2H_6 and CH_3OH production was fairly constant. This resulted in varying C_2H_6 and CH_3OH abundances with respect to H_2O, ranging from ∼0.7% for C_2H_6 and ∼2.2% for CH_3OH on UT January 11 to ∼1% for C_2H_6 and ∼3% for CH_3OH on UT January 12 and 13. However, the water production rate measured in the Lcustom setting on UT January 11 is ∼40% less than the value measured in the M2 setting just hours earlier. Comparing C_2H_6 and CH_3OH to the H_2O production rate derived from Lcustom instead of M2 results in higher mixing ratios that are similar to those measured on UT January 12 and 13. Similarly, on UT January 13, the H_2O production rate measured in Lcustom is ∼20% higher than that measured earlier in the night in the M2 setting. Because of this evidence for temporal variability in H_2O production, on UT January 13, we calculated mixing ratios for species observed in Lp1 (C_2H_6, CH_3OH, and CH_4) to the Lcustom-derived H_2O production rate, for which observations occurred closer in time to the Lp1 setting observations. On UT January 11, the Lp1 observations occurred in between the M2 and Lcustom observations. Therefore, in Table 4, we show mixing ratios compared to both values of the H_2O production rate. The rotation period of the nucleus is ∼9 hr (Farnham et al. 2018), making it plausible that changes in water production could occur on timescales of approximately 4 and 2 hr (as we measure on UT January 11 and 13, respectively) owing to

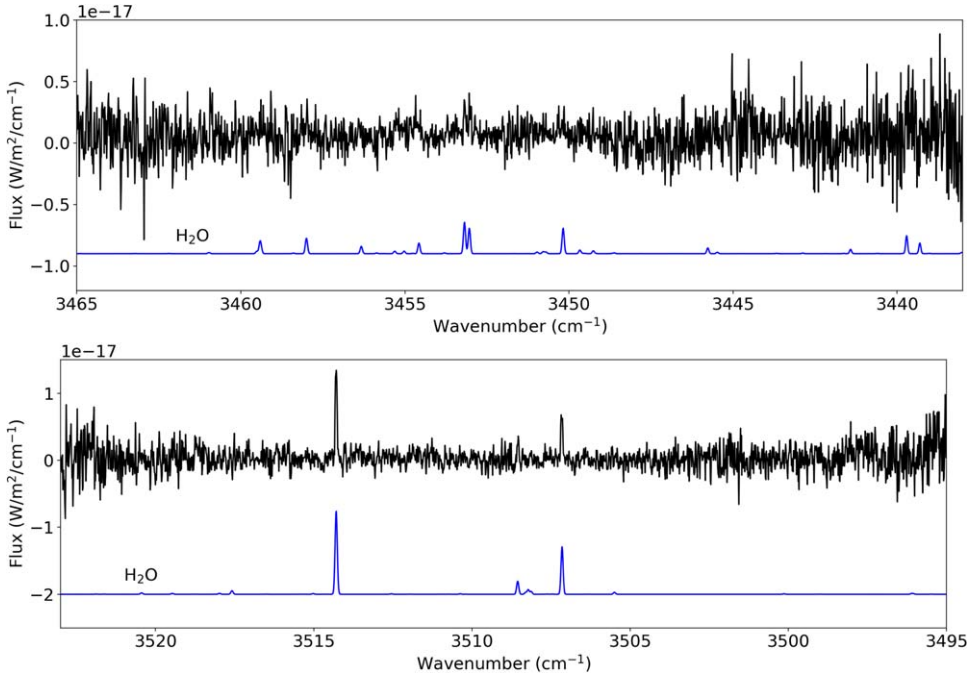

Figure 3. IR spectra from UT January 11 showing spectral regions containing H_2O emissions from our Lcustom setting observations. Data are shown in black, with the model fits for H_2O offset below the spectra for clarity. Combining these spectral regions allows for an independent measure of T_{rot}, as well as another measure of the H_2O production rate, in addition to the lines observed simultaneously with CO.

changing insolation patterns that result from nucleus rotation. However, our data are too sparse to show this definitively.

No CH_4 was detected on any date, with the most sensitive upper limit on the production rate being on UT January 11 and UT January 12. Due to the higher H_2O production rate on UT January 11 (at least as measured in the M2 setting), this resulted in this date providing the most stringent constraint on the CH_4/H_2O ratio of $\lesssim$1%. For the same reason, observations on UT January 11 also provided the most sensitive upper limit on the CO/H_2O ratio, which is ∼0.5%.

3.2. Optical: H_2O and CO_2 from [O I]

The spectral regions around each [O I] line are shown in Figure 4. All lines were clearly detected, though there is some overlap in the cometary and telluric line profiles. Therefore, the line profiles needed to be deblended as discussed in Section 2.2.2.

We measured an oxygen line ratio of 0.075 ± 0.006, a typical value for comets at 1 au from the Sun (Cochran & Cochran 2002; Cochran 2008; Decock et al. 2013). The flux ratio of the [O I] 6300 and [O I] 6364 Å lines is 3.07 ± 0.25, in excellent agreement with previously measured values (e.g., Cochran & Cochran 2002; McKay et al. 2013; Decock et al. 2013), as well as the theoretical value of 3.0 (Sharpee & Slanger 2006; this ratio is set by quantum mechanics and has this value regardless of the parentage of the O I or other factors). The H_2O production rate derived from the [O I] 6300 Å line is $(5.5 \pm 1.0) \times 10^{27}$ mol s^{-1}. For this production rate, we calculated that a scaling factor of 1.37 ± 0.06 was needed to correct for collisional quenching of the [O I] 6300 and [O I] 6364 Å lines. Doing so resulted in a collisionally adjusted oxygen line ratio of 0.054 ± 0.005.

As discussed earlier, [O I] photochemistry in cometary comae is not fully understood, which introduces systematic uncertainty into any attempt to infer the CO_2/H_2O ratio in a cometary coma. To evaluate the systematic uncertainty in our CO_2 abundance estimate, we calculated ratios based on two values of the release rates proposed by McKay et al. (2015) and shown in Table 3. Both of these release rates reproduced the abundance observed in C/2012 K1 (PanSTARRS) to an accuracy of ∼20% (McKay et al. 2016). For 46P, the release rates A and B resulted in $CO_2/H_2O = (9.7 \pm 1.0)\%$ and $(14.7 \pm 1.6)\%$, respectively. In both cases, the uncertainties are purely stochastic and do not attempt to account for systematic uncertainties in the release rates. In a sample of comets with both [O I] and CO_2 observations, we have found that release rates B better reproduce CO_2 abundances in the sample (A. J. McKay et al. 2021, in preparation). Therefore, we favor those rates at this time and adopt $(14.7 \pm 1.6)\%$ as our inferred CO_2/H_2O ratio in 46P. However, with the current (lack of) understanding of O I photochemistry, we conclude that the CO_2 abundance in 46P could be anywhere from 10% to 20%.

3.3. Active Areas

We employed our H_2O and CO_2 production rates and upper limit on the CO production rate to calculate the active areas (or upper limit, in the case of CO) of the cometary surface using the sublimation model of Cowan & A'Hearn (1979); they are given in Table 5. We adopted the slow rotator model, for which every facet of the nucleus surface is in equilibrium with the solar radiation incident upon it (see Bodewits et al. 2014; McKay et al. 2017, 2018, for justification of this model approach). We assumed a bond albedo of 0.04 for the surface. We present the active areas and fractions in Table 5. For calculation of the active fraction, we adopt a sphere with an effective radius of 0.56 km (Boehnhardt et al. 2002). A more recent (but not peer-reviewed as of this writing) size estimate from radar observations is somewhat larger, with a radius of 0.63–0.7 km (https://news.arizona.edu/story/ua-researcher-captures-rare-radar-images-comet-46pwirtanen). Adopting this

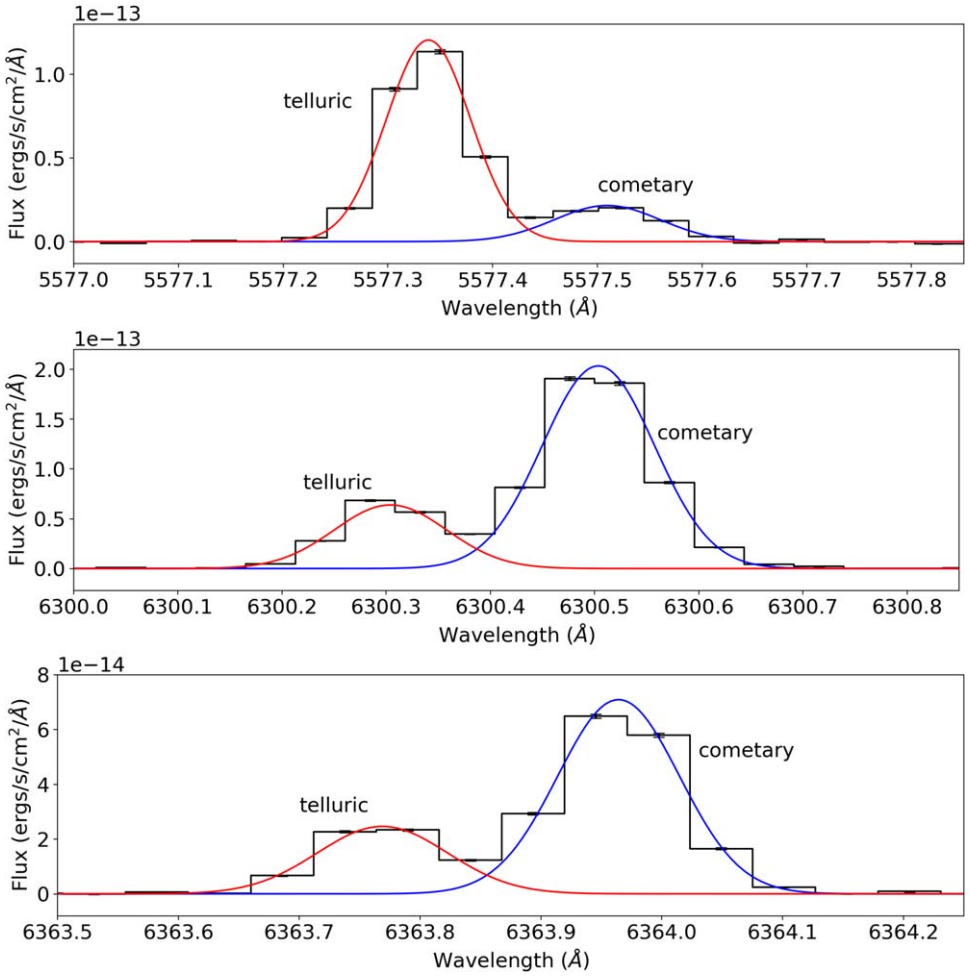

Figure 4. Spectral regions showing the [O I] 5577 Å (top), [O I] 6300 Å (middle), and [O I] 6364 Å (bottom) emission in 46P. The cometary line is redward of the telluric feature, and both components of the line profile are labeled. The telluric and cometary lines are well separated but exhibit some overlap, which is accounted for in our line-fitting methodology. The fits to individual lines are overplotted in red (telluric) and blue (cometary), illustrating the small amount of overlap in the line profiles.

size lowers the corresponding active fractions by a factor of 1.4. While these are simple model assumptions, they are still useful diagnostics for the drivers of activity and comparison to other comets. More detailed modeling (for instance, taking into account the nucleus shape) is beyond the scope of this paper.

Water shows the highest active fraction, on the order of 30%–45%, reflecting the range of water production rates measured in this work. The active fraction of CO_2 is a factor of 10 lower at 3.5%, whereas the CO active fraction is very low, less than 0.04%.

4. Discussion

4.1. Comparison to Other Observations of 46P

Few measurements of the molecules we observed have been reported for 46P. Combi et al. (2020; this issue) reported H_2O production rates based on Lyα observations with SOHO that overlap with our observations and found H_2O production rates of 6–7 $\times$ 10^{27} mol s^{-1}. These values are somewhat higher than our values but may be explained by the vastly different fields of view (FOVs) projected at the comet for our observations (tens to hundreds of kilometers) compared with those of Combi et al. (2020; hundreds of thousands of kilometers) and the potential for an extended source of H_2O production (see Section 4.2).

Combi et al. (2020) also noted that the water production of 46P was lower than previous apparitions, and our observations support that conclusion.

In this special issue, Roth et al. (2021) and Khan et al. (2021) reported on IR observations closer to perihelion in 2018 December. Bonev et al. (2021) also reported on IR observations in 2018 December with Keck NIRSPEC2. These observations were not sensitive to CH_4 and CO because of the small geocentric velocity of the comet (see Section 1), but they do provide observations of H_2O, CH_3OH, and C_2H_6. They found that $C_2H_6/H_2O \sim 0.7\%$–0.8% and $CH_3OH/H_2O \sim 3\%$–4%, with $Q_{H_2O} \sim 6$–9×10^{27} mol s^{-1}. The mixing ratios for CH_3OH are similar to what we measure on UT January 12 and 13 but higher than the values measured on UT January 11 when they are compared to the water production rate derived from the M2 setting (if the Lcustom water production is used, the mixing ratios on UT January 11 also agree with those measured near perihelion). The C_2H_6/H_2O ratio we measured is somewhat higher than at perihelion, except if the UT January 11 observations are ratioed to the water production rate measured in the M2 setting. The water production rate is somewhat higher than our range of values, but considering 3 weeks separate our observations from theirs and the comet moved away from the Sun during that time, a decreasing gas

Table 5
Active Areas and Fractions

Species	Vaporization Rate (10^{17} mol s^{-1} cm^{-2})	Production Rate (10^{27} mol s^{-1})	Active Area (km^2)	Active Fraction (%)
H_2O	3.28	5.70 ± 0.43[a]	1.74 ± 0.13	45 ± 7
H_2O	3.28	3.52 ± 0.44[b]	1.07 ± 0.13	28 ± 5
CO_2	5.90	0.81 ± 0.09	0.14 ± 0.02	3.5 ± 0.7
CO	18.5	<0.031	<0.0017	<0.04

Notes.
[a] Highest value measured in this work.
[b] Lowest value measured in this work.

production rate over this time period is not surprising. Based on the C_2H_6 and CH_3OH abundances, we do not see strong evidence for a long-timescale (seasonal or heliocentric distance related) change in mixing ratios, though the lower values on UT January 11 when compared to the M2-derived water production rate may provide evidence for short-timescale variations, possibly due to rotation, as discussed in Section 3.1.3 for water production.

Submillimeter observations by Coulson et al. (2020) placed a 3σ upper limit on the CO production rate of $Q_{CO} < 9.2 \times 10^{25}$ mol s^{-1} in December near perihelion. For the water production rates of 6–9 $\times$ 10^{27} mol s^{-1} discussed above, this results in an upper limit on the CO/H_2O ratio of approximately 1%–1.5%. Our upper limits are approximately a factor of 2 more sensitive and consistent with the findings of Coulson et al. (2020). Bauer et al. (this issue) reported on NEOWISE observations of CO_2 in 2018 June and 2019 April, with the April epoch being closer in time to our observations. They found a CO_2 production rate of approximately 1 $\times$ 10^{26} mol s^{-1} at $R_h = 1.9$ au. Unfortunately, due to the large separation in time and heliocentric distance, this comparison cannot confirm or refute our inferred CO_2 abundance.

Zheltobryukhov et al. (2020) obtained dust and polarization measurements of 46P on January 12 and 13 within hours of our observations and found a constant V magnitude and polarization on both dates within uncertainties of 10%–20%. While we observe some evidence for different H_2O production rates on these dates (see Table 4), this difference is only on the order of 10%–20%, similar to the uncertainties in the dust measurements. Additionally, the dust measurements were obtained over a much larger projected FOV (5000–10,000 km) than our observations (hundreds of kilometers), meaning the variability that we observe may very well be averaged over in larger FOV observations like those of the dust. Therefore, no firm conclusions about the relationship between H_2O outgassing and dust activity can be reached.

4.2. Active Fractions

Our derived active areas and fractions for H_2O, CO_2, and CO (upper limit) are given in Table 5. The H_2O active fraction is larger than typically observed in comets (<5%; A'Hearn et al. 1995) but is not greater than 100%, meaning 46P is not officially a hyperactive comet from our observations. However, the large active fraction does suggest that additional surface area is being ejected into the coma in the form of icy grains, a concept often invoked to explain large active fractions and hyperactive comets (e.g Lisse et al. 2009; A'Hearn et al. 2011; Kelley et al. 2013; Combi et al. 2014; Bodewits et al. 2014; McKay et al. 2015; Lis et al. 2019). The EPOXI flyby observed direct evidence for these icy grains (A'Hearn et al. 2011; Kelley et al. 2013), firmly establishing icy grains as a probable source of the appearance of hyperactivity in comets. While such a high active fraction seems to contradict our bond albedo assumption, raising the albedo results in a lower surface temperature for the nucleus, meaning water sublimation rates will be lower. This means more active area is required to explain the observed water production rate, reinforcing the interpretation of additional surface area being required. This topic was investigated by McKay et al. (2018), and they reached the same conclusion. The high-CO_2 active fraction, comparable to water active fractions in many comets (e.g., A'Hearn et al. 1995), is consistent with the hypothesis suggested for 103P/Hartley 2 that CO_2 sublimation is responsible for driving out water-rich icy grains (A'Hearn et al. 2011; Kelley et al. 2013), and such a process could be operating on 46P as well. The low-CO active fraction suggests that CO is not an important driver of activity for 46P, consistent with our strongly depleted CO abundance.

4.3. Comparison to Other Comets

We compare 46P to the growing IR taxonomy (Dello Russo et al. 2016) in Table 6 and Figure 5, both to comets as a whole and to JFCs. The C_2H_6 and CH_3OH are enriched, whereas our upper limit is sensitive enough to conclude that CO is depleted. The CH_4 is consistent with being typical or depleted but not likely enriched. Compared to other JFCs, 46P is enriched in C_2H_6 and CH_3OH; however, the CO upper limit is consistent with the small number of measurements in other JFCs, though it is lower than some of the values measured for other JFCs. The inferred CO_2/H_2O ratio is near the mean value of 17% derived by the AKARI survey (Ootsubo et al. 2012), and the CO_2/CO ratio is greater than 27, consistent with many comets observed in the AKARI survey and also similar to fellow hyperactive JFC 103P/Hartley 2.

Considering recent results pertaining to the variability of H_2O production in comets and the presence of extended sources of production (e.g A'Hearn et al. 2011; McKay et al. 2015; DiSanti et al. 2018), an alternative taxonomy is to compare to C_2H_6 rather than H_2O as argued in Bonev et al. (2021). Mixing ratios compared to C_2H_6 are shown in Table 4. Compared to C_2H_6, CH_3OH and CO are depleted in 46P compared to both comets as a whole and JFCs. Our upper limit on CH_4/C_2H_6 of ~1.4 is consistent with this ratio being typical or depleted compared with both the population of comets as a whole and JFCs.

The compositional profile consisting of depleted CO and typical to enhanced C_2H_6 and CH_3OH suggests efficient hydrogenation of molecules such as CO and C_2H_2 on grain

Table 6
46P Compared to Other Comets

	Mixing Ratios X/H_2O (%)			
Comet	C_2H_6	CO	CH_4	CH_3OH
46P/Wirtanen[a]	0.94 ± 0.07	<**0.54**	<0.97	2.99 ± 0.23
JFCs				
2P/Encke[b]	0.32 ± 0.03	<1.77	0.34 ± 0.10	3.48 ± 0.27
2P/Encke[c]	0.037 ± 0.005	0.43 ± 0.04	0.11 ± 0.01	0.87 ± 0.09
9P/Tempel 1[d]	0.29 ± 0.04	4.3 ± 1.0	0.54 ± 0.30	1.4 ± 0.2
21P/Giacobini-Zinner[e]	0.24 ± 0.07	1.99 ± 0.41	<0.89	2.27 ± 0.39
21P/Giacobini-Zinner[f]	0.24 ± 0.01	1.63 ± 0.07	0.63–1.52	…
45P/Honda-Mrkos-Pajdusakova[g]	0.52 ± 0.04	0.60 ± 0.04	0.79 ± 0.06	3.59 ± 0.31
45P/Honda-Mrkos-Pajdusakova[h]	0.81 ± 0.07	<3.7	1.0 ± 0.2	4.51 ± 0.54
73P/Schwassmann-Wachmann-B[i]	0.17 ± 0.01	<1.9	<4.1	0.54 ± 0.11
73P/Schwassmann-Wachmann-C[j]	0.11 ± 0.01	0.53 ± 0.13	<0.25	0.49 ± 0.06
103P/Hartley 2[k]	0.75 ± 0.02	0.15–0.45	<0.47	1.95 ± 0.07
252P/LINEAR[l]	0.95 ± 0.04	<4.43	<3.92	4.87 ± 0.34
Ave. OCC[m]	0.63 ± 0.10	6.1 ± 1.6	0.88 ± 0.10	2.21 ± 0.24

Notes.
[a] Values for 46P from this work represent an average of detections on all three dates. For CH_4, we adopt the most sensitive upper limit obtained on UT January 11.
[b] Radeva et al. (2013), 2003 apparition, preperihelion.
[c] Roth et al. (2018), 2017 apparition, postperihelion.
[d] Mumma et al. (2005).
[e] Faggi et al. (2019), averages over 2018 apparition.
[f] Roth et al. (2020), averages over 2018 apparition.
[g] DiSanti et al. (2017), $R_h = 0.55$ au.
[h] Dello Russo et al. (2020), $R_h = 1.01$–1.10 au.
[i] Dello Russo et al. (2007); Kobayashi et al. (2007).
[j] Villanueva et al. (2006); Dello Russo et al. (2007); DiSanti et al. (2007).
[k] Dello Russo et al. (2011); Mumma et al. (2011); Weaver et al. (2011); Kawakita et al. (2013).
[l] Paganini et al. (2019).
[m] Dello Russo et al. (2016).

surfaces during the protoplanetary disk phase, resulting in the formation of CH_3OH and C_2H_6. The depleted CO is consistent with other JFCs, and this depletion could very well be evolutionary, as JFCs experience many close passages to the Sun compared to their Oort Cloud counterparts. However, DiSanti et al. (2017) argued that because the other hypervolatiles, CH_4 and C_2H_6, were not depleted in 45P/Honda-Mrkos-Pajdusakova (and were enriched compared to values in other JFCs), the depletion of CO was indeed primordial, as CH_4 and C_2H_6 could be lost via similar processes. Our upper limit on CH_4 does not allow us to conclude whether CH_4 is typical or depleted in 46P, but the typical to enriched C_2H_6 abundance means a similar argument for the CO depletion being primordial could be applied to 46P as well. In addition, the typical CO_2 abundance observed provides additional evidence for limited evolutionary influence on 46P's current coma composition.

4.4. Comparison to 103P/Hartley 2: A Sibling Comet?

A particularly compelling comparison for 46P is to JFC 103P/Hartley 2, flyby target of the EPOXI mission (A'Hearn et al. 2011). Comparisons have often been made between 46P and 103P because of their small size and hyperactivity. Using measured H_2O production rates from the 2010 apparition (Combi et al. 2011; Dello Russo et al. 2011) and the measured surface area of 103P from the EPOXI mission (A'Hearn et al. 2011), the active fraction is ∼50%, similar to the value we find for 46P. More recently, evidence supporting their similarity has become even more pronounced. Both comets have exhibited similar secular changes in water production over the past 20 yr (Combi et al. 2020, this issue). Both have terrestrial-like D/H ratios in H_2O (Hartogh et al. 2011; Lis et al. 2019). This work has revealed that they also have similar volatile abundances. The CO_2/H_2O ratio observed by the EPOXI spacecraft varied between 10% and 20% (A'Hearn et al. 2011), encompassing the range of values inferred for 46P from our [O I] observations, even accounting for systematic uncertainties introduced by the lack of knowledge of [O I] photochemistry. The CO abundance was 0.15%–0.45% in 103P (Weaver et al. 2011), placing it firmly in the CO-depleted class of comets, like 46P. The C_2H_6 abundances compared to H_2O for 103P range from 0.6% to 1.0%, whereas the CH_3OH abundances range from 1% to 3% (Dello Russo et al. 2011; Mumma et al. 2011; Kawakita et al. 2013), again similar to the range of abundances we observe in 46P. Their similar $H_2O/CO_2/CO$ abundance ratios combined with their large H_2O and CO_2 active fractions point to similar drivers of activity.

Could 46P and 103P be the best-studied members of a subfamily of JFCs with similar composition, size, and activity drivers? And if so, are there other members waiting to be studied? Comet 45P/Honda-Mrkos-Pajdusakova is a candidate as a hyperactive comet with a terrestrial D/H ratio (Lis et al. 2013). Although its CO, CH_3OH, and C_2H_6 abundances are similar to both 103P and 46P, the CO_2 abundance is not known, and it has not experienced the same fading over the last 20 yr that 46P and 103P have (Combi et al. 2020, this issue). It is also unclear whether such a compositional family would be

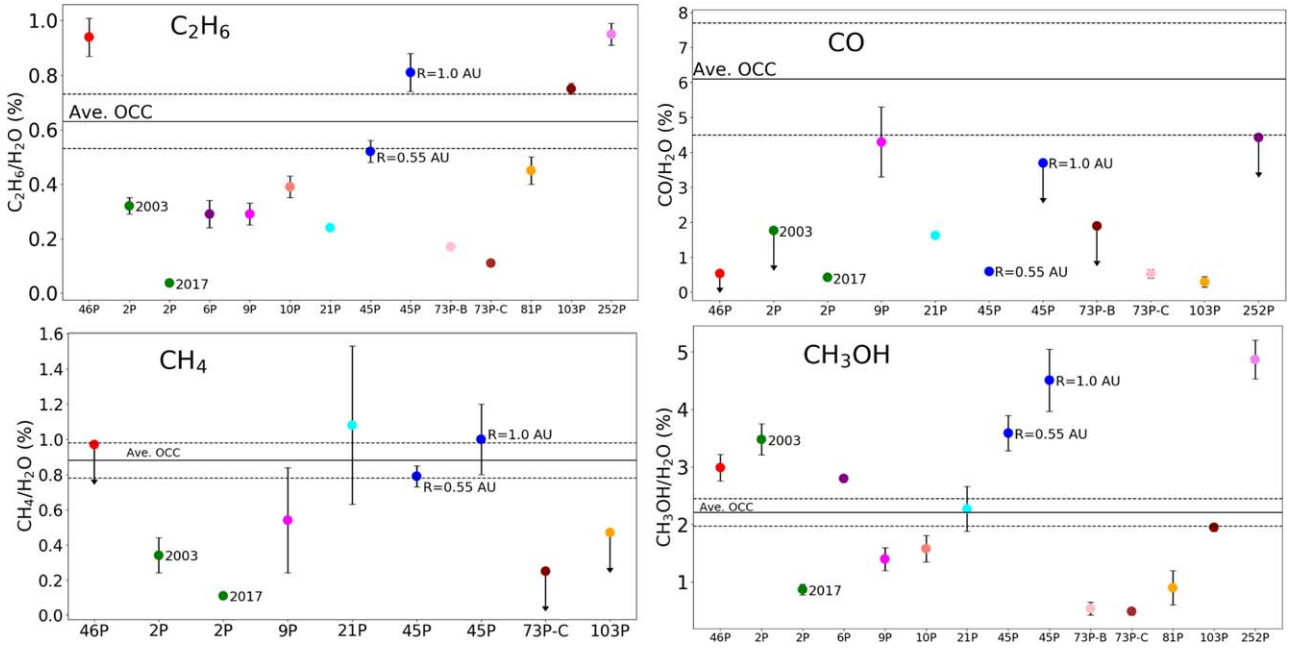

Figure 5. Comparison of C_2H_6 (top left), CO (top right), CH_4 (bottom left), and CH_3OH (bottom right) abundances in 46P to other JFCs and the average value of OCCs. In each panel, the average value of OCCs is shown as a solid horizontal line with two dashed lines above and below signifying the standard deviation in values. Uncertainties are not plotted for points where the uncertainty is smaller than the plotting symbol. For 2P/Encke and 45P, two values are given for different observational circumstances as labeled. As found previously, many JFCs are depleted in C_2H_6 compared to OCCs, but there are exceptions, with 46P being among them. The CH_4 has a similar picture, with some JFCs being depleted but others being typical; CH_3OH exhibits a large scatter in JFCs, from enriched to depleted; and CO is almost universally depleted in the JFCs measured to date, with the possible exception of 9P/Tempel 1, whose uncertainties overlap with the typical range. References are the same as in Table 6, with additional C_2H_6 and CH_3OH values taken from the following: 6P/d'Arrest (Dello Russo et al. 2009), 10P/Tempel 2 (Paganini et al. 2012), and 81P/Wild 2 (Dello Russo et al. 2014).

tracing an ancient breakup of a larger object or whether this reflects similar disk chemistry in a certain part of the protosolar disk. The answer to this distinction has implications for how many objects may be in this compositional family or how the existence of such a family is interpreted. More studies are needed to see if the striking similarity between 103P and 46P is coincidental or reflects a common origin and whether there are other comets with similar compositional/activity profiles. For instance, a more direct measure of the CO_2/CO and CO_2/H_2O ratios (as opposed to the values we report inferred from the oxygen line ratio) from a facility such as the James Webb Space Telescope (JWST) would provide a more accurate measure of these ratios. A mission to 46P would provide the in situ characterization that exists for 103P, such as observational confirmation of an icy grain halo surrounding the nucleus (A'Hearn et al. 2011; Kelley et al. 2013), correlation of CO_2 with dust/ice emission (A'Hearn et al. 2011), and detailed shape and surface properties (e.g., Groussin et al. 2013), but is not available for 46P. Ground-based IR observations of other JFCs will be critical for identifying other comets with compositions similar to 46P and 103P, particularly for the understudied hypervolatiles CO and CH_4 highlighted in this work. Direct observations of CO_2 from space-borne assets, as well as inferred values from ground-based oxygen line ratio measurements in JFCs, are also vital to this effort.

5. Conclusions

This work presents optical and IR spectroscopy of JFC 46P/Wirtanen obtained in 2019 January, 1 month after perihelion. Although these observations were not taken when the comet was at peak brightness, the geocentric velocity at this time was favorable for studies of CH_4, CO, and [O I] emission, conditions that were not achieved near perihelion/closest approach to Earth in 2018 December. Therefore, this provided a rare opportunity to observe the hypervolatiles CH_4 and CO in a JFC.

We determined that CO is depleted in 46P, similar to the small number of JFCs measured to date. Our upper limit on CH_4 rules out an enriched composition but is not sensitive enough to determine whether CH_4 is depleted in 46P. In addition to CH_4 and CO, we presented abundances of C_2H_6 and CH_3OH, both of which are enriched in 46P and had abundances similar to those measured in 2018 December near perihelion. We found evidence for a variable H_2O production rate on the order of hours to days, possibly due to rotation of the nucleus.

From the O I observations, we inferred a CO_2/H_2O ratio of $\sim$15%, similar to many comets observed in the AKARI survey (Ootsubo et al. 2012). Combined with our IR CO measurements, this implies a high CO_2/CO ratio for 46P, similar to another hyperactive JFC, 103P/Hartley 2.

We also derived active fractions for H_2O, CO_2, and CO sublimation based on a simple sublimation model. Although our observations suggest that 46P is no longer technically hyperactive (i.e., active fraction >100%), the active fraction for H_2O is still quite high and indicative of sublimation from an extended source, such as water-rich icy grains.

Lastly, we noted the striking similarity between 46P and 103P/Hartley 2, from their similar small size and high activity to their similar compositional profiles, in terms of both volatiles and isotopic ratios (Hartogh et al. 2011; Lis et al. 2019).

The authors recognize and acknowledge the very significant cultural role and reverence that the summit of Maunakea has always had within the indigenous Hawaiian community. We

are most fortunate to have the opportunity to conduct observations from this mountain. A.J.M. acknowledges support from the NASA Solar System Observations Program through grant 18-SSO18_2-0040 and the Solar System Workings Program through grant 80NSSC20K0140. B.P.B. acknowledges support from NSF Astronomy and Astrophysics grants 1616306 and 2009398. B.P.B., N.D.R., and R.J.V. acknowledge support from the NASA SSO program through grant 80NSSC17K0705; M.A.D. acknowledges support though grant 18-SSO18_2-0040; and A.L.C. acknowledges support through NNX17AI86G. E.G. and N.D.R. acknowledge support from the NASA Emerging Worlds (80NSSC20K0341) and NSF Astronomy and Astrophysics (2009910) programs. N.X.R. acknowledges support from the NASA Postdoctoral Program at the NASA Goddard Space Flight Center, administered by the Universities Space Research Association under contract with NASA, and from NASA Headquarters under the NASA Earth and Space Science Fellowship Program (grant NNX16AP49H)

Some of the observations reported in this paper were obtained at the McDonald Observatory, operated by the University of Texas at Austin. The McDonald Observatory observations were supported by NASA grant NNX17AI86G.

Facilities: NASA IRTF iSHELL, McDonald Observatory.

ORCID iDs

Adam J. McKay https://orcid.org/0000-0002-0622-2400
Michael A. DiSanti https://orcid.org/0000-0001-8843-7511
Anita L. Cochran https://orcid.org/0000-0003-4828-7787
Boncho P. Bonev https://orcid.org/0000-0002-6391-4817
Neil Dello Russo https://orcid.org/0000-0002-8379-7304
Ronald J. Vervack, Jr. https://orcid.org/0000-0002-8227-9564
Erika Gibb https://orcid.org/0000-0003-0142-5265
Nathan X. Roth https://orcid.org/0000-0002-6006-9574
Mohammad Saki https://orcid.org/0000-0003-2277-6232
Younas Khan https://orcid.org/0000-0003-4773-2674
Hideyo Kawakita https://orcid.org/0000-0003-2011-9159

References

A'Hearn, M. F., Belton, M. J. S., Delamere, W. A., et al. 2011, Sci, 332, 1396
A'Hearn, M. F., Millis, R. L., Schleicher, D. G., Osip, D. J., & Birch, P. V. 1995, Icar, 118, 223
Bauer, J. M., Stevenson, R., Kramer, E., et al. 2015, ApJ, 814, 85
Bhardwaj, A., & Raghuram, S. 2012, ApJ, 748, 13
Biver, N., Bockelée-Morvan, D., Crovisier, J., et al. 1999, AJ, 118, 1850
Bockelée-Morvan, D., & Biver, N. 2017, PTRSA, 375, 20160252
Bodewits, D., Farnham, T. L., A'Hearn, M. F., et al. 2014, ApJ, 786, 48
Boehnhardt, H., Delahodde, C., Sekiguchi, T., et al. 2002, A&A, 387, 1107
Bonev, B. P., Dello Russo, N., DiSanti, M. A., et al. 2021, PSJ, in press
Bonev, B. P., DiSanti, M. A., Villanueva, G. L., et al. 2014, ApJL, 796, L6
Bonev, B. P., Mumma, M. J., DiSanti, M. A., et al. 2005, BAAS, 37, 644
Cochran, A. 2008, Icar, 198, 181
Cochran, A., & Cochran, W. 2002, Icar, 157, 297
Combi, M. R., Bertaux, J.-L., Quémerais, E., Ferron, S., & Mäkinen, J. T. T. 2011, ApJL, 734, L6
Combi, M. R., Mäkinen, J. T., Bertaux, J. L., Quémerais, E., & Ferron, S. 2014, AAS, DPS Meeting, 46, 110.09
Combi, M. R., Mäkinen, T., Bertaux, J. L., et al. 2020, PSJ, 1, 72
Coulson, I. M., Liu, F.-C., Cordiner, M. A., et al. 2020, AJ, 160, 182
Cowan, J. J., & A'Hearn, M. F. 1979, M&P, 21, 155
Decock, A., Jehin, E., Hutsemékers, D., & Manfroid, J. 2013, A&A, 555, A34
Dello Russo, N., DiSanti, M. A., Mumma, M. J., Magee-Sauer, K., & Rettig, T. W. 1998, Icar, 135, 377
Dello Russo, N., Kawakita, H., Bonev, B. P., et al. 2020, Icar, 335, 113411
Dello Russo, N., Kawakita, H., Vervack, R. J., & Weaver, H. A. 2016, Icar, 278, 301
Dello Russo, N., Mumma, M., DiSanti, M., et al. 2006, Icar, 184, 255
Dello Russo, N., Vervack, R. J., Kawakita, H., et al. 2014, Icar, 238, 125
Dello Russo, N., Vervack, R. J., Weaver, H. A., et al. 2007, Natur, 448, 172
Dello Russo, N., Vervack, R. J., Jr., Lisse, C. M., et al. 2011, ApJL, 734, L8+
Dello Russo, N., Vervack, R. J., Jr., Weaver, H. A., et al. 2009, ApJ, 703, 187
DiSanti, M. A., Anderson, W. M., Villanueva, G. L., et al. 2007, ApJL, 661, L101
DiSanti, M. A., Bonev, B. P., Dello Russo, N., et al. 2017, AJ, 154, 246
DiSanti, M. A., Bonev, B. P., Gibb, E. L., et al. 2018, AJ, 156, 258
DiSanti, M. A., Villanueva, G. L., Paganini, L., et al. 2014, Icar, 228, 167
Faggi, S., Mumma, M. J., Villanueva, G. L., Paganini, L., & Lippi, M. 2019, AJ, 158, 254
Farnham, T. L., Knight, M. M., Schleicher, D. G., et al. 2018, CBET, 4571, 1
Festou, M., & Feldman, P. 1981, A&A, 103, 154
Fink, U. 2009, Icar, 201, 311
Gibb, E. L., Bonev, B. P., Villanueva, G., et al. 2012, ApJ, 750, 102
Gibb, E. L., Mumma, M. J., Dello Russo, N., DiSanti, M. A., & Magee-Sauer, K. 2003, Icar, 165, 391
Groussin, O., Sunshine, J. M., Feaga, L. M., et al. 2013, Icar, 222, 580
Hartogh, P., Lis, D. C., Bockelée-Morvan, D., et al. 2011, Natur, 478, 218
Haser, L. 1957, BSRSL, 43, 740
Huebner, W., Keady, J., & Lyon, S. 1992, Ap&SS, 195, 1
Huestis, D. L., Bougher, S. W., Fox, J. L., et al. 2008, SSRv, 139, 63
Kawakita, H., Kobayashi, H., Dello Russo, N., et al. 2013, Icar, 222, 723
Kelley, M. S., Lindler, D. J., Bodewits, D., et al. 2013, Icar, 222, 634
Khan, Y., Gibb, E. L., Bonev, B. P., et al. 2021, PSJ, 2, 20
Kobayashi, H., Kawakita, H., Mumma, M. J., et al. 2007, ApJL, 668, L75
Lis, D. C., Biver, N., Bockelée-Morvan, D., et al. 2013, ApJL, 774, L3
Lis, D. C., Bockelée-Morvan, D., Güsten, R., et al. 2019, A&A, 625, L5
Lisse, C. M., Fernandez, Y. R., Reach, W. T., et al. 2009, PASP, 121, 968
McKay, A. J., Bodewits, D., & Li, J.-Y. 2017, Icar, 286, 308
McKay, A. J., Chanover, N. J., DiSanti, M. A., et al. 2014, Icar, 231, 193
McKay, A. J., Chanover, N. J., Morgenthaler, J. P., et al. 2012, Icar, 220, 277
McKay, A. J., Chanover, N. J., Morgenthaler, J. P., et al. 2013, Icar, 222, 684
McKay, A. J., Cochran, A. L., Dello Russo, N., & DiSanti, M. A. 2020, ApJL, 889, L10
McKay, A. J., Cochran, A. L., DiSanti, M. A., et al. 2015, Icar, 250, 504
McKay, A. J., Cochran, A. L., DiSanti, M. A., et al. 2018, Icar, 309, 1
McKay, A. J., DiSanti, M. A., Kelley, M. S. P., et al. 2019, AJ, 158, 128
McKay, A. J., Kelley, M. S. P., Cochran, A. L., et al. 2016, Icar, 266, 249
Morgenthaler, J., Harris, W., Scherb, F., et al. 2001, ApJ, 563, 451
Mumma, M. J., Bonev, B. P., Villanueva, G. L., et al. 2011, ApJL, 734, L7
Mumma, M. J., DiSanti, M. A., Magee-Sauer, K., et al. 2005, Sci, 310, 270
Ootsubo, T., Kawakita, H., Hamada, S., et al. 2012, ApJ, 752, 15
Paganini, L., Camarca, M. N., Mumma, M. J., et al. 2019, AJ, 158, 98
Paganini, L., Mumma, M. J., Boehnhardt, H., et al. 2013, ApJ, 766, 100
Paganini, L., Mumma, M. J., Villanueva, G. L., et al. 2012, ApJL, 748, L13
Radeva, Y. L., Mumma, M. J., Villanueva, G. L., et al. 2013, Icar, 223, 298
Radeva, Y. L., Mumma, M. J., Villanueva, G. L., & A'Hearn, M. F. 2011, ApJ, 729, 135
Raghuram, S., Hutsemékers, D., Opitom, C., et al. 2020, A&A, 635, A108
Rayner, J., Bond, T., Bonnet, M., et al. 2012, Proc. SPIE, 8446, 84462C
Rayner, J., Tokunaga, A., Jaffe, D., et al. 2016, Proc. SPIE, 9908, 990884
Reach, W. T., Kelley, M. S., & Vaubaillon, J. 2013, Icar, 226, 777
Roth, N. X., Bonev, B. P., DiSanti, M. A., et al. 2021, PSJ, in press
Roth, N. X., Gibb, E. L., Bonev, B. P., et al. 2018, AJ, 156, 251
Roth, N. X., Gibb, E. L., Bonev, B. P., et al. 2020, AJ, 159, 42
Sharpee, B., & Slanger, T. 2006, JPCA, 110, 6707
Tull, R. G., MacQueen, P. J., Sneden, C., & Lambert, D. L. 1995, PASP, 107, 251
Villanueva, G. L., Bonev, B. P., Mumma, M. J., et al. 2006, ApJL, 650, L87
Villanueva, G. L., DiSanti, M. A., Mumma, M. J., & Xu, L. H. 2012a, ApJ, 747, 37
Villanueva, G. L., Mumma, M. J., Bonev, B. P., et al. 2012b, JQSRT, 113, 202
Villanueva, G. L., Mumma, M. J., DiSanti, M. A., et al. 2011a, Icar, 216, 227
Villanueva, G. L., Mumma, M. J., & Magee-Sauer, K. 2011b, JGRE, 116, E08012
Weaver, H. A., Feldman, P. D., A'Hearn, M. F., Dello Russo, N., & Stern, S. A. 2011, ApJL, 734, L5
Zheltobryukhov, M., Zubko, E., Chornaya, E., et al. 2020, MNRAS, 498, 1814